

# Induced-field enhancement of band-structure effects in photoelectron spectra from Al surfaces by ultrashort laser pulses

C. A. Ríos Rubiano and R. Della Picca

*CONICET and Centro Atómico Bariloche (CNEA), Bariloche, Argentina*

D. M. Mitnik

*Instituto de Astronomía y Física del Espacio (IAFE, CONICET-UBA), Casilla de correo 67, sucursal 28, C1428EGA Buenos Aires, Argentina and Facultad de Ciencias Exactas y Naturales, Universidad de Buenos Aires, Buenos Aires, Argentina*

V. M. Silkin

*Donostia International Physics Center (DIPC), 20018 San Sebastián, Spain; Departamento de Física de Materiales, Facultad de Ciencias Químicas, Universidad del País Vasco, Apartado 1072, 20080 San Sebastián, Spain; and IKERBASQUE, Basque Foundation for Science, 48011 Bilbao, Spain*

M. S. Gravielle

*Instituto de Astronomía y Física del Espacio (IAFE, CONICET-UBA), Casilla de correo 67, sucursal 28, C1428EGA Buenos Aires, Argentina (Received 29 September 2016; revised manuscript received 30 December 2016; published 3 March 2017)*

The electron emission produced by the grazing incidence of ultrashort laser pulses on two faces of aluminum, Al(100) and Al(111), is investigated using the band-structure-based-Volkov (BSB-V) approximation. The present version of the BSB-V approach includes not only a realistic description of the surface interaction, accounting for band-structure effects, but also effects due to the induced potential that originates from the collective response of valence electrons to the external electromagnetic field. For both crystallographic orientations we found that the induced potential contributes to the emergence of band-structure signatures in the near-threshold region of photoelectron spectra. This result opens a window to scrutinize band-structure effects in metal surfaces via ultrashort-laser interactions.

DOI: [10.1103/PhysRevA.95.033401](https://doi.org/10.1103/PhysRevA.95.033401)

## I. INTRODUCTION

In the last decade, the photoelectron emission (PE) from metal surfaces has received renewed attention as a result of the technological achievement of lasers with pulse durations of the order of attoseconds, which make it possible to study the behavior of electrons in condensed matter at their natural temporal orders [1–7]. Such remarkable experimental progress needs to be accompanied by intensive theoretical research since the underlying quantum processes involve complex many-body mechanisms, whose complete understanding is still far from being achieved [8–14].

When an ultrashort laser pulse interacts with a metal surface, the external electromagnetic field induces not only direct PE from the metal but also collective oscillations of valence electrons, i.e., plasmon excitations. Such a collective response of the metal surface gives rise to a time-dependent induced surface (IS) potential, which affects electron emission spectra [14–20]. This article focuses on the role played by the IS potential to reveal signatures of the surface-band structure in electron distributions from two different crystallographic orientations of aluminum: Al(100) and Al(111).

One of the most remarkable effects of the crystal band structure is the presence of partially occupied surface electronic states (SEs), which display a highly localized electron density at the edge of the crystal surface. For the Be(0001) surface, noticeable SES signatures were found in electron distributions produced by ultrashort laser pulses with high carrier frequencies [21], for which the contribution of the IS

potential was assumed to be negligible. But for aluminum, the typical metal surface, weak surface-band structure effects were observed when the IS potential was not included in the calculations [21]. Precisely, in this work we find that the contribution of the IS potential is essential to make visible band-structure marks in the low-energy region of PE spectra from aluminum surfaces. This feature is observed even for high-frequency laser pulses, for which valence electrons are expected not to be able to follow the fast oscillations of the external perturbation.

To describe the PE process we have made use of a time-dependent distorted-wave method named the band-structure-based-Volkov (BSB-V) approximation [21]. The BSB-V approach includes an accurate description of the electron-surface interaction, given by the band-structure-based (BSB) model [22], while the action of the laser field on the emitted electron is represented by means of the Volkov phase [23]. The BSB model is based on the one-dimensional pseudopotential by Chulkov *et al.* [22,24], which takes into account the electronic structure of the surface, replicating the width and position of the projected bulk energy gap and the surface and first image electronic states [25–29]. It has been successfully applied to different PE processes [11,12,21]. In contrast to our previous calculations [21], in this version of the BSB-V approach we have incorporated the contribution of the IS interaction through a perturbative potential and a Volkov-type phase. The induced potential has been derived in a consistent way from the unperturbed BSB electronic states by using a linear response theory [30].

The BSB-V approximation, including the dynamic IS contribution, has been applied to evaluate double-differential (energy- and angle-resolved) PE distributions for Al(100) and Al(111). For these surfaces, the influence of partially occupied SESs as well as the IS potential has been examined by varying the carrier frequency of the laser pulse. This article is organized as follows: In Sec. II we introduce the extended version of the BSB-V approximation, which takes into account the effect of the IS potential; in Sec. III results are shown and discussed, while our conclusions are summarized in Sec. IV. Atomic units are used unless otherwise stated.

## II. THEORETICAL METHOD

Let us consider a finite laser pulse, characterized by a time-dependent electric field  $\mathbf{F}_L(t)$ , grazing impinging on a metal surface  $S$ . As a consequence of the interaction, a valence electron, initially in the state  $\Phi_i$ , is ejected above the vacuum level, reaching a final state  $\Phi_f$ . Within the framework of the time-dependent distorted wave formalism [31], the BSB-V transition amplitude for the electronic transition  $\Phi_i \rightarrow \Phi_f$  reads [21]

$$\mathcal{A}_{if} = -i \int_{-\infty}^{+\infty} dt \langle \chi_f^{(\text{BSBV})}(\mathbf{r}, t) | \mathcal{V}(\mathbf{r}, t) | \Phi_i(\mathbf{r}, t) \rangle, \quad (1)$$

where

$$\mathcal{V}(\mathbf{r}, t) = \mathbf{r} \cdot \mathbf{F}_L(t) + V_{\text{IS}}(\mathbf{r}, t) \quad (2)$$

is the perturbative potential at time  $t$  and  $\chi_f^{(\text{BSBV})}(\mathbf{r}, t)$  is the final BSB-V distorted wave function, with  $\mathbf{r}$  being the position vector of the active electron. The first term of Eq. (2) represents the interaction potential with the laser, expressed in the length gauge, while the second term,  $V_{\text{IS}}$ , denotes the IS potential that is produced by electronic density fluctuations caused by the external field. The frame of reference is placed at the position of the crystal border, which is shifted outward with respect to the position of the topmost atomic layer by half of the interplanar distance, with the  $\hat{\mathbf{z}}$  axis being oriented normal to the surface, pointing towards the vacuum region.

Within the BSB-V approach, the unperturbed states  $\Phi_i$  and  $\Phi_f$  are solutions of the Schrödinger equation associated with the one-dimensional electron-surface potential  $V_S(z)$  given by Ref. [24], which depends on  $z$ , the component of  $\mathbf{r}$  perpendicular to the surface plane. Hence, the states  $\Phi_i \equiv \Phi_{\mathbf{k}_s, n_i}(\mathbf{r}, t)$  and  $\Phi_f \equiv \Phi_{\mathbf{k}_s, n_f}(\mathbf{r}, t)$  can be expressed as

$$\Phi_{\mathbf{k}_s, n}(\mathbf{r}, t) = \frac{1}{2\pi} \exp(i\mathbf{k}_s \cdot \mathbf{r}_s) \phi_n(z) e^{-iEt}, \quad (3)$$

where  $\mathbf{k}_s$  ( $\mathbf{r}_s$ ) is the component of the electron momentum (position vector) parallel to the surface plane;  $\phi_n(z)$  is the one-dimensional eigenfunction, with eigenenergy  $\varepsilon_n$ , derived from the potential  $V_S(z)$ ; and  $E = k_s^2/2 + \varepsilon_n$  is the total electron energy.

According to the grazing incidence condition and the translational invariance of the problem in the plane parallel to the surface, the laser field is linearly polarized perpendicular to the surface, that is,  $\mathbf{F}_L(t) = F_L(t)\hat{\mathbf{z}}$ . The temporal profile of the pulse reads

$$F_L(t) = F_0 \sin(\omega t + \varphi) \sin^2(\pi t/\tau) \quad (4)$$

for  $0 < t < \tau$  and vanishes at all other times. In Eq. (4)  $F_0$  represents the maximum field strength,  $\omega$  is the carrier frequency,  $\tau$  is the pulse duration, and  $\varphi$  is the carrier envelope phase, which is defined as  $\varphi = (\pi - \omega\tau)/2$  for symmetric pulses. In this work we consider laser pulses with a fixed number  $N$  of full cycles inside the envelope; then, the pulse duration is defined as  $\tau = NT$ , with  $T = 2\pi/\omega$  being the laser oscillation period.

The induced potential  $V_{\text{IS}}$  is evaluated from a linear response theory based on the BSB wave functions of Eq. (3) [32]. Making use of a slab geometry to derive the one-dimensional wave functions  $\phi_n(z)$ , the induced field  $\mathbf{F}_{\text{IS}} = -\nabla_{\mathbf{r}} V_{\text{IS}}(\mathbf{r}, t)$  can be nearly expressed as

$$\mathbf{F}_{\text{IS}}(z, t) \cong \begin{cases} F_{\text{IS}}(t) \hat{\mathbf{z}} & \text{for } -d < z < 0, \\ 0 & \text{otherwise,} \end{cases} \quad (5)$$

where  $d$  is the width of the slab, formed by a sufficiently large number of atomic layers of the metallic crystal. The function

$$F_{\text{IS}}(t) = -\frac{1}{2\pi} \int_{-\infty}^{\infty} d\nu \tilde{F}_L(\nu) f_{\text{IS}}(\nu) e^{-i\nu t} \quad (6)$$

is the IS field inside the metal at time  $t$ , with  $\tilde{F}_L(\nu)$  denoting the Fourier transform of  $F_L(t)$ . In Eq. (6) the function  $f_{\text{IS}}(\nu)$  is related to the dynamic response induced by a unitary and monochromatic electric field of frequency  $\nu$ . By neglecting the weak oscillatory dependence of the induced field inside the metal on  $z$ , the function  $f_{\text{IS}}(\nu)$  can be derived from

$$v_{\text{IS}}(z, \nu) = 4\pi \int_z^0 dz' \int_{z_0}^{z'} dz'' \rho_{\text{ind}}(z'', \nu) \simeq z f_{\text{IS}}(\nu) \quad (7)$$

for  $z \leq 0$ , where  $v_{\text{IS}}(z, \nu)$  is the potential induced in the crystal by the external potential  $v_{\text{ext}}(\mathbf{r}, \nu) = -(2\pi/q_s) \exp(i\mathbf{q}_s \cdot \mathbf{r}_s + q_s z) \exp(i\nu t)$  for  $q_s \rightarrow 0$ ,  $\rho_{\text{ind}}(z, \nu)$  is the corresponding dynamical induced charge density, and  $z_0$  is a fixed reference distance. In the linear-response theory  $\rho_{\text{ind}}(z, \nu)$  is expressed as

$$\rho_{\text{ind}}(z, \nu) = \int dz' \chi(z, z', q_s, \nu) v_{\text{ext}}(z', q_s, \nu), \quad (8)$$

where  $\chi$  is the density-response function for interacting electrons. It is a solution of the integral equation  $\chi = \chi^o + \chi v \chi^o$ , where  $\chi^o$  is the density-response function of noninteracting electrons and  $v$  is, in the random-phase approximation, the bare Coulomb potential. The noninteracting response function is derived from the single-particle energies  $\varepsilon_n$  and wave functions  $\phi_n(z)$  according to

$$\chi^o(z, z', q_s, \nu) = \frac{2}{S} \sum_{n, n'} \phi_n(z) \phi_{n'}^*(z) \phi_n^*(z') \phi_{n'}(z') \times \sum_{\mathbf{k}} \frac{f_{\mathbf{k}_s, n} - f_{\mathbf{k}_s + \mathbf{q}_s, n'}}{E_{\mathbf{k}_s, n} - E_{\mathbf{k}_s + \mathbf{q}_s, n'} + \nu + i\eta}, \quad (9)$$

where  $S$  is the normalization area, the sums over  $n$  and  $n'$  involve both the occupied and unoccupied states,  $f_{\mathbf{k}_s, n}$  is the Fermi occupation factor, and  $\eta$  is infinitesimal. Further calculation details can be found in Ref. [32].

From Eqs. (2) and (5) it is possible to build  $\chi_f^{(\text{BSBV})}(\mathbf{r}, t)$  by introducing the distortions of both the external and induced

fields in the momentum distribution of the final state  $\Phi_{\mathbf{k}_{f_s}, n_f}$  by means of a Volkov-type phase [17,21,33]. It reads

$$\chi_f^{(\text{BSBV})}(\mathbf{r}, t) = \Phi_{\mathbf{k}_{f_s}, n_f}(\mathbf{r} - \hat{\mathbf{z}} \alpha_L(t), t) \times \exp[iz A_{\text{tot}}(z, t) - i\beta_L(t)], \quad (10)$$

where the function

$$A_{\text{tot}}(z, t) = \begin{cases} A_L(t) + A_{\text{IS}}(t) & \text{for } -d < z < 0, \\ A_L(t) & \text{otherwise,} \end{cases} \quad (11)$$

represents the position-dependent total vector potential at time  $t$ , with

$$A_\mu(t) = - \int_{+\infty}^t dt' F_\mu(t'), \quad \mu = L, \text{IS}, \quad (12)$$

being the vector potentials, with incoming asymptotic conditions associated with the laser ( $\mu = L$ ) and induced surface ( $\mu = \text{IS}$ ) fields. In turn, the functions

$$\alpha_L(t) = \int_{+\infty}^t dt' A_L(t') \quad (13)$$

and

$$\beta_L(t) = \frac{1}{2} \int_{+\infty}^t dt' [A_L(t')]^2, \quad (14)$$

involved in Eq. (10), are respectively related to the quiver amplitude and the ponderomotive energy of the laser.

Finally, by replacing Eqs. (2), (3), and (10) in Eq. (1), the BSB-V transition amplitude, including the induced contribution, reduces to  $\mathcal{A}_{if} = \delta(\mathbf{k}_{f_s} - \mathbf{k}_{i_s}) a_{if}$ , where the Dirac delta function imposes the momentum conservation in the plane parallel to the surface and

$$a_{if} = -i \int_0^{+\infty} dt R_{if}(t) e^{i[\Delta \varepsilon t + \beta_L(t)]} \quad (15)$$

represents the one-dimensional transition amplitude, with  $\Delta \varepsilon = \varepsilon_{n_f} - \varepsilon_{n_i}$  being the energy gained by the electron during the process. The function  $R_{if}$  denotes the form factor given by

$$R_{if}(t) = \int_{-\infty}^{+\infty} dz \phi_{n_f}^*[z - \alpha_L(t)] \phi_{n_i}(z) g_f(z) \mathcal{V}(z, t) \times \exp[-i z A_{\text{tot}}(z, t)], \quad (16)$$

where  $g_f(z) = e^{z\Theta(-z)/\lambda_f}$  accounts for the stopping of the ionized electron inside the material [21], with  $\Theta$  being the unitary Heaviside function and  $\lambda_f = \lambda(E_f)$  being the electron mean free path as a function of the final electron energy  $E_f = k_{f_s}^2/2 + \varepsilon_{n_f}$ .

Analogous to Ref. [21], the BSB-V differential probability of PE from the surface-state band can be expressed in terms of the one-dimensional transition amplitude of Eq. (15) as

$$\frac{d^2 P}{dE_f d\Omega_f} = 2k_f \rho(k_{f_z}) \sum_{n_i} |a_{if}|^2 \Theta(\tilde{k}_{n_i} - k_{f_s}), \quad (17)$$

where  $\Omega_f$  is the solid angle determined by the final electron momentum  $\mathbf{k}_f = \mathbf{k}_{f_s} + k_{f_z} \hat{\mathbf{z}}$ , with  $k_{f_z} = \sqrt{2\varepsilon_{n_f}}$ . The angle  $\Omega_f$  is defined as  $\Omega_f = (\theta_f, \varphi_f)$ , where  $\theta_f$  and  $\varphi_f$  are, respectively, the polar and azimuthal angles, with  $\theta_f$  measured with respect to the surface plane. In Eq. (17), the sum indicates the addition over all the  $\phi_{n_i}$  states with energies  $\varepsilon_{n_i} \leq -E_W$

( $E_W$  is the function work),  $\rho(k_{f_z})$  is the density of final states  $\phi_{n_f}$  with perpendicular momentum  $k_{f_z}$ , and the factor 2 takes into account the spin states. The Heaviside function  $\Theta(\tilde{k}_{n_i} - k_{f_s})$  comes from the momentum conservation in the direction parallel to the surface plane, with  $\tilde{k}_{n_i} = \sqrt{-2(\varepsilon_{n_i} + E_W)}$ .

### III. RESULTS

We apply the BSB-V approximation to simulate PE distributions from the valence electron system of Al(100) and Al(111). Since the ejection parallel to the polarization vector of the laser field is expected to provide the major contribution to the PE rate [21], in this article we study only electron emission normal to the surface plane, i.e.,  $\theta_f = 90^\circ$ . The maximum field strength was chosen to be  $F_0 = 10^{-3}$  a.u. (intensity  $I_L = 3.52 \times 10^{10}$  W/cm<sup>2</sup>), which belongs to the perturbative range, far from the damage threshold of the material [34]. In relation to the pulse duration, laser pulses containing  $N = 6$  cycles inside the envelope are considered along the work. However, the main features of the low-energy spectra are slightly dependent on  $\tau$ , being similar for different few-cycle pulses.

The BSB-V differential probability was evaluated from Eq. (17) by varying the carrier frequency of the laser pulse. In the calculation, the BSB wave functions  $\phi_n(z)$  were numerically derived by expanding them onto a basis of plane waves, defined as

$$\{\exp[i2\pi j(z + d/2)/D], j = -n_0, \dots, n_0\},$$

where  $2n_0 + 1$  is the number of basis functions and  $D$  is the unit-cell width, which acts as a normalization length. By using such an expansion in Eq. (16), the form factor  $R_{if}(t)$  was reduced to a closed form in terms of the laser and induced fields, while the numerical integration over time involved in Eq. (15) was done with a relative error lower than 1%. Moreover, taking into account that the functions  $\phi_{n_f}$  do not allow us to distinguish ionized electrons moving with negative normal velocities (i.e., towards the bulk) from those moving towards the vacuum region, to evaluate the emission probability we averaged the contributions from the two different wave functions associated with the same positive energy  $\varepsilon_{n_f}$  by considering that ionized electrons emitted towards the vacuum region represent approximately 50% of the total ionized electrons from the valence electron system [21,35].

The parameters associated with the different orientations of aluminum are the following: The Al(100) surface presents a work function  $E_W = 0.161$  a.u. and an interplanar distance of 3.80 a.u., while the corresponding BSB wave functions  $\phi_n(z)$  were obtained by using a basis of plane waves with  $n_0 = 220$ , a unit-cell width  $D = 342.04$  a.u., and a slab width  $d = 266.00$  a.u. (i.e., 71 atomic layers). The Al(111) surface is characterized by a work function  $E_W = 0.156$  a.u. and an interplanar distance of 4.39 a.u. The corresponding  $\phi_n(z)$  wave functions were evaluated using a plane-wave basis with  $n_0 = 170$ ,  $D = 394.92$  a.u., and  $d = 307.16$  a.u. (i.e., 71 atomic layers). Both faces of aluminum display the same Fermi energy,  $E_F = 0.41$  a.u., and therefore the same surface plasmon frequency  $\omega_s = 0.40$  a.u., which characterizes the collective motion of valence electrons. The energy-dependent

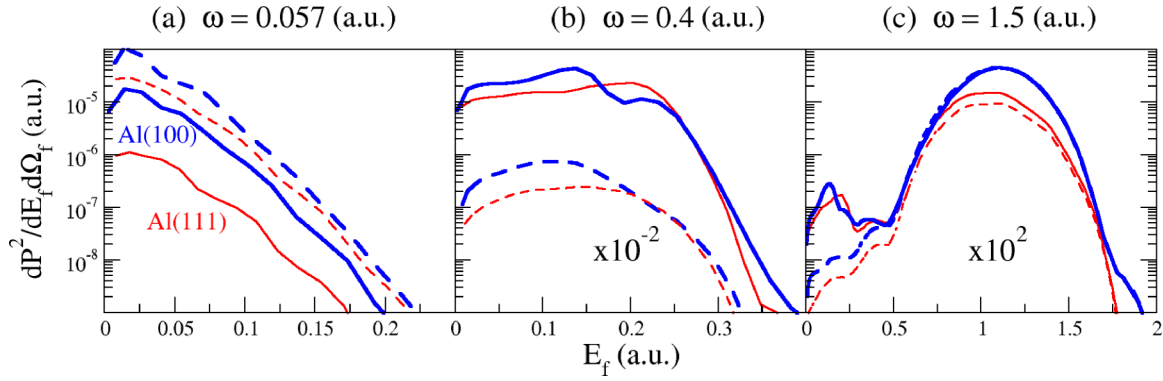


FIG. 1. PE probabilities in the normal direction (i.e.,  $\theta_f = 90^\circ$ ) as a function of the final electron energy  $E_f$ . Each panel corresponds to a different carrier frequency of the laser pulse:  $\omega = 0.057$ , 0.4, and 1.5 a.u. from left to right, respectively. In all the panels, BSB-V results with (without) the inclusion of the IS potential are displayed by thick solid (dashed) blue line for Al(100) and with the thin solid (dashed) red line for Al(111).

electron mean free path  $\lambda(E_f)$  was interpolated from data corresponding to the aluminum bulk, extracted from Ref. [36].

First, in order to provide an overall picture of the influence of the aluminum crystal face, in Fig. 1 we compare PE distributions from Al(100) and Al(111) produced by laser pulses with different carrier frequencies,  $\omega = 0.057$ , 0.4, and 1.5 a.u., which are displayed in different panels. BSB-V results with and without the contribution of the IS potential are shown in all the panels. These latter BSB-V values, without the IS potential, were derived from Eq. (17) by fixing  $F_{IS}(t) = A_{IS}(t) = 0$ .

In Fig. 1(a), for the carrier frequency  $\omega = 0.057$  a.u., corresponding to the Ti:sapphire laser system, the PE distribution from the Al(100) surface is about one order of magnitude higher than the one corresponding to the Al(111) face. But the intensity differences between PE probabilities from both aluminum faces decrease significantly when the IS potential is neglected. On the other hand, when  $\omega$  increases, becoming equal to or larger than surface plasmon frequency, emission probabilities from the two crystallographic orientations are comparable in magnitude, departing appreciably from each other only around the main maximum for high carrier frequencies, as it happens for  $\omega = 1.5$  a.u. [Fig. 1(c)]. However, a closer examination of the spectra in Figs. 1(b) and 1(c) reveals the presence of additional low-energy structures, which depend on the crystal face. While for  $\omega = 0.4$  a.u. such structures arise as superimposed bulges on the main maximum, for  $\omega = 1.5$  a.u. they correspond to a further peak placed in the near-threshold region of the spectrum. Noteworthy, these structures completely disappear when the IS contribution is not taken into account. Therefore, the goal of the paper is to scrutinize the origin of such crystallographic effects in the low-energy region of PE spectra, i.e., at  $E_f \lesssim 0.3$  a.u., focusing on the influence of the IS potential.

Before addressing the study of aluminum crystal-face effects in detail, it is convenient to discuss the general features of the PE distributions in Fig. 1. These electron spectra are governed by the multiphoton mechanism associated with a Keldysh parameter  $\gamma = \omega\sqrt{E_W}/F_0$  greater than the unity, in which the carrier frequency of the laser pulse approximates to the photon energy. Consequently, for the higher frequencies,  $\omega = 0.4$  and 1.5 a.u., the distributions in Fig. 1 display a broad

maximum resulting from the absorption of one photon of energy  $\omega$ , which corresponds to the first of the above-threshold-ionization (ATI) peaks. The first ATI maximum is roughly placed at  $E_f \simeq \langle E_i \rangle - U_p + \omega$ , where  $\langle E_i \rangle$  is the initial energy averaged over all initial states, with  $\langle E_i \rangle \simeq -0.44$  and  $-0.43$  a.u. for Al(100) and Al(111), respectively, and  $U_p = F_0^2/(4\omega^2)$  is the ponderomotive energy, which is negligible in the present cases. Due to the uncertainty principle, the width of the ATI peaks depends on the pulse duration, decreasing as  $\tau$  increases [17], like observed in atomic photoionization [37]. However, in contrast to the atomic case, the electron emission from metal surfaces presents a lower limit of the width of the ATI peaks, which is produced by the energy spread of the metal valence electrons, characterized by the Fermi energy. This fact causes the absence of ATI structures in the multiphoton spectra for  $\omega = 0.057$  a.u. [Fig. 1(a)] because the energy difference between consecutive ATI peaks is much lower than the width of each peak. Hence, PE distributions for low carrier frequencies present a smoothly decreasing intensity as the velocity of ejected electrons increases, with this behavior being practically independent of the pulse duration.

In view of the fact that the crystal-face effects observed in the low-energy region of the PE distributions of Fig. 1 can be traced from SES and IS contributions, both will be separately analyzed in the following sections.

### A. Partial contribution from SESs

As a consequence of the high electron density of the SESs near the surface border, which favors the release of electrons from the material, SESs are expected to provide an important contribution to PE yields. In the case of aluminum, the (100) and (111) faces present similar work functions but very different corrugations of the potential  $V_S(z)$ . In Fig. 2 we plot the surface potential  $V_S(z)$  for Al(100) and Al(111), together with the square modulus of the corresponding SESs  $|\phi_{SES}(z)|^2$ , with eigenenergies  $\varepsilon_{SES} = -0.263$  a.u. and  $\varepsilon_{SES} = -0.32$  a.u., respectively. From Fig. 2 it is clear that the average depth of the potential well, defined as  $V_{S0} = E_F + E_W$ , is almost the same for both orientations. However, the corrugation of  $V_S(z)$  for the (100) face is about a factor of 6 larger than the one corresponding to the (111) orientation. Precisely, this

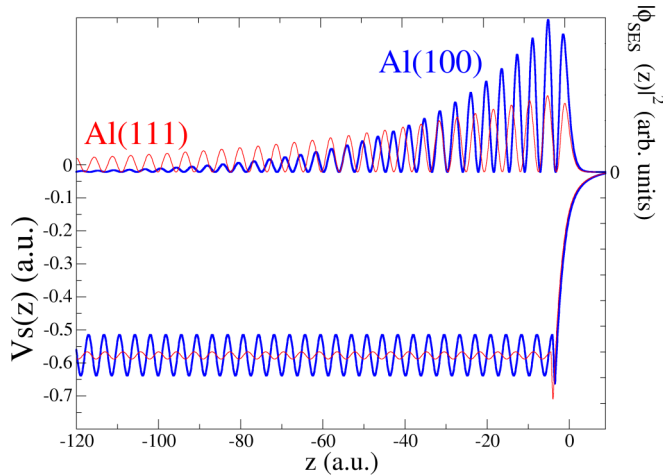


FIG. 2. Potential  $V_S(z)$  (lower graph), together with the square modulus of the corresponding SESs  $|\phi_{\text{SES}}(z)|^2$  (upper graph), with thick blue lines for Al(100) and thin red lines for Al(111).

stronger corrugation of the Al(100) potential affects the surface electronic density. Therefore, although both surfaces present partially occupied SESs with energies in the vicinity of the Fermi level, the localization of the electron density near the crystal border is more than 2 times higher for Al(100) than for Al(111), affecting the corresponding PE distributions.

For the lowest frequency,  $\omega = 0.057$  a.u., in Figs. 3(a) and 3(b) we compare differential emission probabilities for Al(100) and Al(111), respectively, with partial values due to emission from SESs as well as from states at the top of the occupied states (TOSs). While TOS probabilities are similar for the two orientations, partial contributions coming from SESs are about two orders of magnitude higher for the (100) face than for the (111) one. For this latter orientation, SES emission is lower than that corresponding to TOSs, becoming concealed by emissions from other initial states, but for the (100) face the SES contribution largely dominates the near-threshold region of the electron distribution. Then, for low carrier frequencies we found that the marked difference between the SES densities of both aluminum faces at the

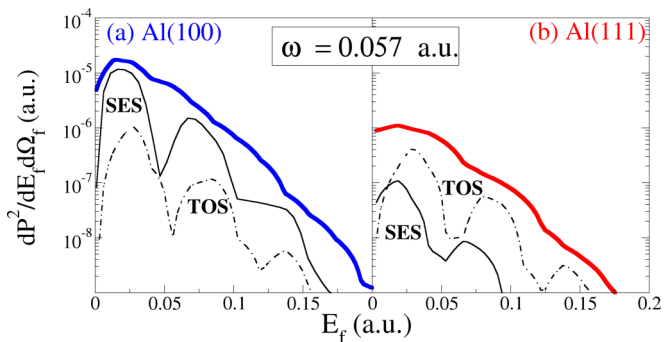


FIG. 3. PE distribution in the normal direction as a function of the final electron energy for (a) Al(100) and (b) Al(111). The carrier frequency of the laser pulse is  $\omega = 0.057$  a.u. In both panels, BSB-V results, including the IS potential, are displayed with thick solid lines; partial contributions from partially occupied SESs and TOSs are plotted with thin solid and dot-dashed black lines, respectively.

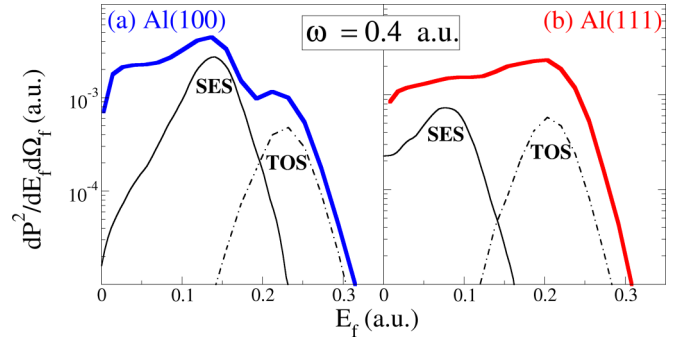
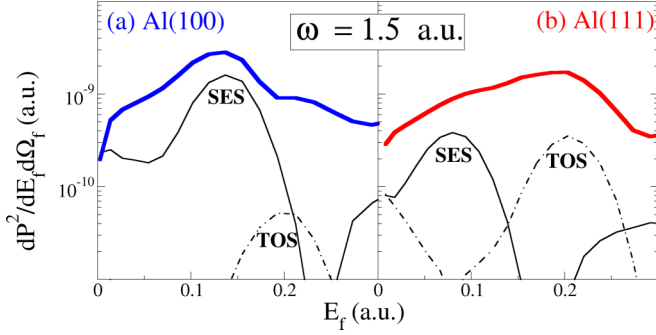


FIG. 4. The same as Fig. 3 for  $\omega = 0.4$  a.u.

surface border is reflected by the intensity difference of the PE probabilities at low energies.

The situation is different for the resonant case in which the carrier frequency of the laser pulse coincides with the surface plasmon frequency. In Fig. 4, for  $\omega \simeq \omega_s = 0.4$  a.u. we compare differential PE probabilities corresponding to the two aluminum faces with partial SES and TOS contributions. For the (100) orientation the first ATI peak displays a double-bump structure, with two bulges peaking at  $E_f \approx 0.14$  a.u. and  $E_f \approx 0.24$  a.u., whereas for (111) only one maximum at  $E_f \approx 0.24$  a.u. exists. The maximum at  $E_f \approx 0.24$  a.u., present for the two faces, corresponds to one-photon absorption from partially occupied TOSs, being situated at  $E_f \simeq -E_W + \omega$ . Instead, the peak at  $E_f \sim 0.14$  a.u., visible only in the Al(100) spectrum, is produced by the absorption of one photon from partially occupied SESs, being placed at  $E_f \simeq \varepsilon_{\text{SES}} + \omega$ . From the comparison of Figs. 4(a) and 4(b) we conclude that the presence or absence of SES signatures in the PE distribution, depending on the crystal face, is once again associated with the major or minor localization of the electronic density of SESs at the crystal border. For the (100) face the high localization makes SES emission clearly discernible in the PE spectrum, while for the (111) face the SES contribution is comparable to emission from other initially occupied states, which partially conceals the footprints of SESs in the electron distribution. Therefore, PE spectra under resonant conditions might offer an attractive window to obtain information about the surface band structure. In addition, in the resonant case the contribution of the plasmon decay mechanism should also be included, producing an additional structure just at the electronic energy  $E_f \simeq \omega_s$ , out of the energy range studied in the present work.

Band-structure effects disappear as the carrier frequency departs from  $\omega_s$ , but remarkably, they become visible again for high carrier frequencies, as shown in Fig. 5. In this case, SES and TOS contributions emerge as superimposed structures in the near-threshold region, being different for the two crystallographic orientations. Again, the low-energy hump due to ejection of slow electrons from TOSs is visible for both faces, while the one associated with emission from SESs is clearly perceptible only for the (100) face. As discussed above, this is a consequence of the different corrugations of the two crystallographic orientations. Furthermore, even though for high frequencies these low-energy structures are less noticeable than in the resonant case, they might still

FIG. 5. The same as Fig. 3 for  $\omega = 1.5$  a.u.

provide information about the relative importance of SES and TOS contributions.

### B. Influence of the IS potential

The band-structure effects discussed in Sec. III A strongly depend on the presence of the IS potential. In turn, since the collective reaction of valence electrons to the external field varies markedly with the carrier frequency, this wide variation of the induced response is directly reflected in the IS contribution to the electron emission yield.

For near-infrared carrier frequencies, like  $\omega = 0.057$  a.u., the slow oscillations of the laser pulse allow valence electrons to react promptly to the external perturbation. Then, at each time the induced response screens the laser field in the aluminum almost completely, tending to the static limit in which the total electric field inside the metal is null (see inset of Fig. 6). Hence, the inclusion of the induced potential causes a marked reduction of the PE yield, as illustrated for Al(111) in Fig. 6. In Fig. 6, in order to assess the importance of band-structure effects for the (111) orientation, we also

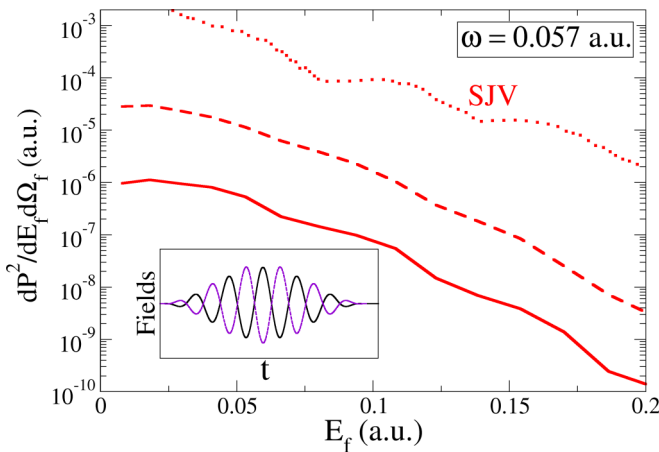


FIG. 6. PE distribution from Al(111) as a function of the final electron energy for a laser pulse with a carrier frequency  $\omega = 0.057$  a.u. The solid (dashed) red line shows BSB-V results with (without) the inclusion of the IS potential; the dotted red line shows SJV results from Ref. [17]. Inset: Corresponding laser and IS fields as a function of the time  $t$  are plotted with solid black and dashed violet lines, respectively.

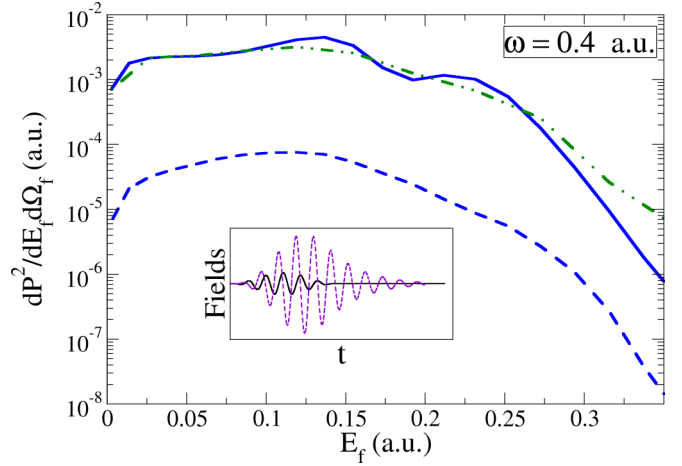


FIG. 7. The same as Fig. 6 for Al(100) and a carrier frequency  $\omega = 0.4$  a.u. BSB-V results neglecting the postcollision interaction, as explained in the text, are displayed with dot-dashed green line.

show the PE distribution derived within the surface jellium-Volkov (SJV) approach [17], where the surface interaction is represented by a simple step potential (jellium model). Even though the SJV approximation includes the contribution of the IS field in a consistent way, SJV results largely overestimate BSB-V probabilities, evidencing the relevance of band-structure contributions in the near-threshold region of PE spectra. Concerning the influence of the IS potential on the crystal-orientation effects observed in Fig. 3, note that the strong screening of the external field inside the metal, as a consequence of the presence of  $F_{IS}(t)$ , mainly affects excitations from initial states whose electron densities are localized in the bulk. This fact enhances the relative contribution of partially occupied SESs, which present a nonnegligible electron density in the selvedge region, just in the region where the IS field vanishes.

When the frequency increases to the resonant value  $\omega \simeq \omega_s = 0.4$  a.u., the maximum strength of  $F_{IS}(t)$  becomes 4 times larger than  $F_0$  (see inset of Fig. 7). Therefore, the

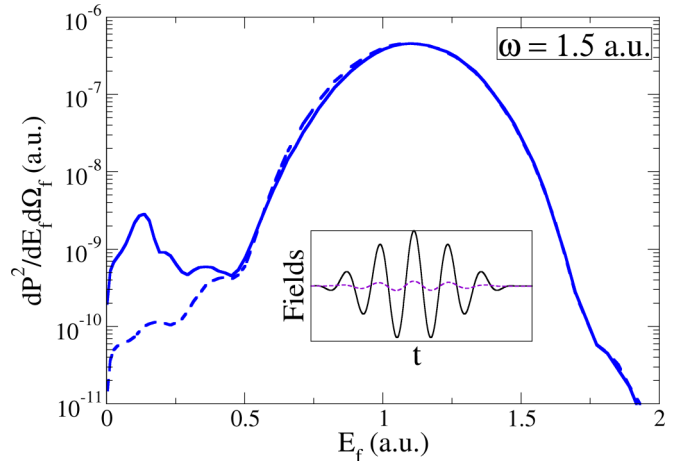


FIG. 8. The same as Fig. 6 for Al(100) and a carrier frequency  $\omega = 1.5$  a.u.

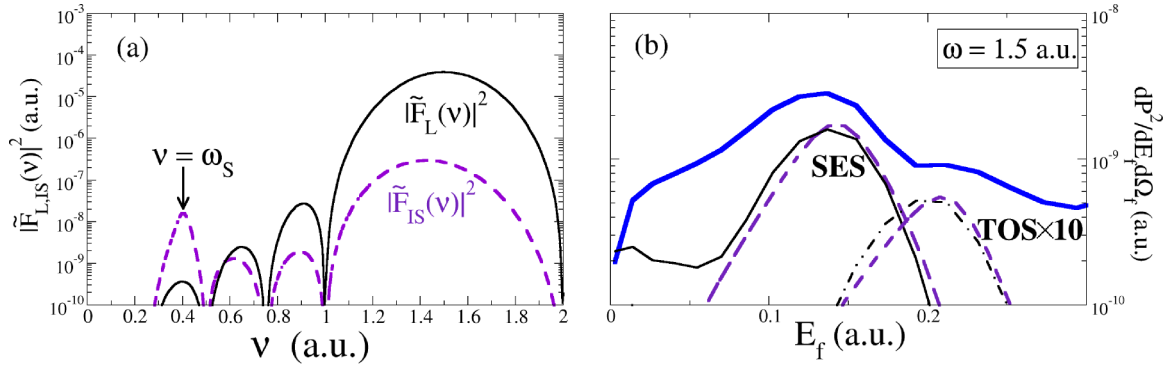


FIG. 9. Analysis of the frequency domain distribution of partial contributions to PE spectra from the valence electrons of Al(100). The carrier frequency of the laser pulse is  $\omega = 1.5$  a.u. (a) Frequency profiles of the laser and induced fields as a function of the frequency. The solid black (dashed violet) line shows the Fourier transform of the laser field  $\tilde{F}_L$  (IS field  $\tilde{F}_{IS}$ ). The vertical arrow indicates the frequency  $\nu = \omega_s$ . (b) PE distribution as a function of the electron energy. The thick solid blue line shows BSB-V results for valence electron emission; the thin solid (dot-dashed) black line shows the SES (TOS) contribution. Fourier transform contributions  $|\tilde{F}_{\text{tot}}(E_f + \epsilon_{\text{SES}})|^2$  and  $|\tilde{F}_{\text{tot}}(E_f + \epsilon_{\text{TOS}})|^2$  (in arbitrary units) are plotted with dashed violet lines.

total field inside the metal becomes dominated by the induced response of the aluminum, giving rise to a large increase in the emission probability, greater than two orders of magnitude, as observed in Fig. 7 for Al(100). For this resonant frequency, the induced field not only is higher than the external field but also persists two times longer than the original pulse duration, contributing to increasing the emission probability after the laser field turns off. Indeed, this postcollision IS interaction after time  $\tau$  produces the enhancement of the band-structure effects. When this postcollision contribution is not taken into account, that is, replacing the upper limit of the integral in Eq. (15) by  $\tau$ , the bumps corresponding to the SES and TOS partial emissions disappear completely from the PE spectrum of Al(100), as displayed in Fig. 7. This effect is related to the fact that under the action of the IS field alone, slow electrons placed close to the interface have a better chance to be released without suffering collisions inside the material.

Finally, the case of  $\omega = 1.5$  a.u., shown in Fig. 8, deserves further discussion. For such a high frequency, electrons are not able to follow the quick variation of the external perturbation, and consequently, the maximum strength of  $F_{IS}(t)$  is more than one order of magnitude lower than that of the laser field (see inset of Fig. 8). Therefore, this small induced response does not affect appreciably the main electron emission, which occurs around the first ATI peak. However, we remarkably found that the IS potential introduces a pronounced growth of the probability at low electron energies just in the region where the double-hump low-energy structure appears in the PE spectrum of Al(100). To investigate thoroughly this unforeseen low-energy contribution for  $\omega = 1.5$  a.u., in Fig. 9(a) we plot the decomposition in frequencies of both the laser [ $\tilde{F}_L(\nu)$ ] and IS [ $\tilde{F}_{IS}(\nu)$ ] fields for this case. The utility of analyzing the frequency domain of the fields lies in the fact that the PE spectrum can be roughly estimated as being proportional to the square modulus of the Fourier transform of the total electric field, that is,  $|\tilde{F}_{\text{tot}}(\nu)|^2$ , evaluated at  $\nu = E_f + E_i$ , with  $\tilde{F}_{\text{tot}}(\nu) = \tilde{F}_L(\nu) + \tilde{F}_{IS}(\nu)$  and  $E_i$  covering the energy range of all initially occupied states. From Fig. 9(a), although the Fourier transform of the laser field is several orders of

magnitude higher than that of the induced field around the carrier frequency,  $\tilde{F}_{IS}(\nu)$  retains a peak associated with the resonance at  $\nu \cong \omega_s$ , which largely exceeds the value of  $\tilde{F}_L(\omega_s)$ . This resonant peak is found to be the origin of the low-energy SES and TOS bulges of the spectrum, as shown in Fig. 9(b), where we observe that the curves corresponding to  $|\tilde{F}_{\text{tot}}(E_f + \epsilon_{\text{SES}})|^2$  and  $|\tilde{F}_{\text{tot}}(E_f + \epsilon_{\text{TOS}})|^2$  (multiplied by an arbitrary factor) almost coincide with the SES and TOS contributions, respectively.

#### IV. CONCLUSIONS

We have studied PE spectra produced by the interaction of ultrashort laser pulses with the valence electrons of two different faces of aluminum, Al(100) and Al(111), using the BSB-V approximation. In the present version of the BSB-V approach we have incorporated the contribution of the induced field, that is originated the collective response of surface electrons to the external perturbation. We have found that the induced response of the metal surface strongly affects electron emission distributions, bringing crystal-orientation effects to light. For the (100) face the IS contribution makes visible near-threshold signatures coming from partially occupied SESs and TOSs. On the other hand, for the (111) orientation the SES structures are almost completely washed out by emission from other initially occupied states, and only the TOS emission can be distinguished in the low-energy region of the PE spectra. These findings open the way to investigate band-structure effects by focusing on the near-threshold region of the electron distributions.

#### ACKNOWLEDGMENTS

Financial support from CONICET, UBA, and ANPCyT of Argentina is acknowledged. V.M.S. acknowledges the partial support from the FIS2016-76617-P.

- [1] A. L. Cavalieri, N. Muller, Th Uphues, V. S. Yakovlev, A. Baltuska, B. Horvath, B. Schmidt, L. Blumel, R. Holzwarth, S. Hendel, M. Drescher, U. Kleineberg, P. M. Echenique, R. Kienberger, F. Krausz, and U. Heinzmann, Attosecond spectroscopy in condensed matter, *Nature (London)* **449**, 1029 (2007).
- [2] L. Miaja-Avila, C. Lei, M. Aeschlimann, J. L. Gland, M. M. Murnane, H. C. Kapteyn, and G. Saathoff, Laser-Assisted Photoelectric Effect from Surfaces, *Phys. Rev. Lett.* **97**, 113604 (2006).
- [3] L. Miaja-Avila, G. Saathoff, S. Mathias, J. Yin, C. La-o vorakiat, M. Bauer, M. Aeschlimann, M. M. Murnane, and H. C. Kapteyn, Direct Measurement of Core-Level Relaxation Dynamics on a Surface-Adsorbate System, *Phys. Rev. Lett.* **101**, 046101 (2008).
- [4] G. Saathoff, L. Miaja-Avila, M. Aeschlimann, M. M. Murnane, and H. C. Kapteyn, Laser-assisted photoemission from surfaces, *Phys. Rev. A* **77**, 022903 (2008).
- [5] L. Miaja-Avila, J. Yin, S. Backus, G. Saathoff, M. Aeschlimann, M. M. Murnane, and H. C. Kapteyn, Ultrafast studies of electronic processes at surfaces using the laser-assisted photoelectric effect with long-wavelength dressing light, *Phys. Rev. A* **79**, 030901 (2009).
- [6] S. Neppel, R. Ernstorfer, E. M. Bothschafter, A. L. Cavalieri, D. Menzel, J. V. Barth, F. Krausz, R. Kienberger, and P. Feulner, Attosecond Time-Resolved Photoemission from Core and Valence States of Magnesium, *Phys. Rev. Lett.* **109**, 087401 (2012).
- [7] S. Neppel, R. Ernstorfer, A. L. Cavalieri, C. Lemell, G. Wachter, E. Magerl, E. M. Bothschafter, M. Jobst, M. Hofstetter, U. Kleineberg, J. V. Barth, D. Menzel, J. Burgdorfer, P. Feulner, F. Krausz, and R. Kienberger, Direct observation of electron propagation and dielectric screening on the atomic length scale, *Nature (London)* **517**, 342 (2015).
- [8] M. N. Faraggi, M. S. Gravielle, and D. M. Mitnik, Interaction of ultrashort laser pulses with metal surfaces: Impulsive jellium-Volkov approximation versus the solution of the time-dependent Schrödinger equation, *Phys. Rev. A* **76**, 012903 (2007).
- [9] J. C. Baggesen and L. B. Madsen, Theory for time-resolved measurements of laser-induced electron emission from metal surfaces, *Phys. Rev. A* **78**, 032903 (2008).
- [10] E. E. Krasovskii, Attosecond spectroscopy of solids: Streaking phase shift due to lattice scattering, *Phys. Rev. B* **84**, 195106 (2011).
- [11] A. G. Borisov, D. Sánchez-Portal, A. K. Kazansky, and P. M. Echenique, Resonant and nonresonant processes in attosecond streaking from metals, *Phys. Rev. B* **87**, 121110 (2013).
- [12] Q. Liao and U. Thumm, Attosecond Time-Resolved Photoelectron Dispersion and Photoemission Time Delays, *Phys. Rev. Lett.* **112**, 023602 (2014).
- [13] C. Lemell, S. Neppel, G. Wachter, K. Tókési, R. Ernstorfer, P. Feulner, R. Kienberger, and J. Burgdorfer, Real-time observation of collective excitations in photoemission, *Phys. Rev. B* **91**, 241101 (2015).
- [14] H. Jouin, M. Raynaud, G. Duchateau, G. Geoffroy, A. Sadou, and P. Martin, Quantum-classical model for the surface plasmon enhanced photoemission process at metal surfaces, *Phys. Rev. B* **89**, 195136 (2014).
- [15] J. Kupersztych, P. Monchicourt, and M. Raynaud, Ponderomotive Acceleration of Photoelectrons in Surface-Plasmon-Assisted Multiphoton Photoelectric Emission, *Phys. Rev. Lett.* **86**, 5180 (2001).
- [16] S. E. Irvine and A. Y. Elezzabi, Surface-plasmon-based electron acceleration, *Phys. Rev. A* **73**, 013815 (2006).
- [17] M. Faraggi, I. Aldazabal, M. S. Gravielle, A. Arnau, and V. M. Silkin, Study of the induced potential produced by ultrashort pulses on metal surfaces, *J. Opt. Soc. Am. B* **26**, 2331 (2009).
- [18] E. E. Krasovskii, V. M. Silkin, V. U. Nazarov, P. M. Echenique, and E. V. Chulkov, Dielectric screening and band-structure effects in low-energy photoemission, *Phys. Rev. B* **82**, 125102 (2010).
- [19] P. Földi, I. Márton, N. Német, V. Ayadi, and P. Dombi, Few-cycle plasmon oscillations controlling photoemission from metal nanoparticles, *Appl. Phys. Lett.* **106**, 013111 (2015).
- [20] N. Fedorov, G. Geoffroy, G. Duchateau, L. Štolcová, J. Proška, F. Novotný, M. Domonkos, H. Jouin, P. Martin, and M. Raynaud, Enhanced photoemission from laser-excited plasmonic nano-objects in periodic arrays, *J. Phys. Condens. Matter* **28**, 315301 (2016).
- [21] C. A. Rios Rubiano, M. S. Gravielle, D. M. Mitnik, and V. M. Silkin, Band-structure effects in photoelectron-emission spectra from metal surfaces, *Phys. Rev. A* **85**, 043422 (2012).
- [22] E. V. Chulkov, V. M. Silkin, and P. M. Echenique, Image potential states on metal surfaces: Binding energies and wave functions, *Surf. Sci.* **437**, 330 (1999).
- [23] D. M. Wolkow, Über eine klasse von lasungen der diracschen gleichung, *Z. Phys.* **94**, 250 (1935).
- [24] E. V. Chulkov, V. M. Silkin, and P. M. Echenique, Image potential states on lithium, copper and silver surfaces, *Surf. Sci.* **391**, L1217 (1997).
- [25] P. M. Echenique and J. B. Pendry, The existence and detection of Rydberg states at surfaces, *J. Phys. C* **11**, 2065 (1978).
- [26] F. Finocchi, C. M. Bertoni, and S. Ossicini, Simple metal-surfaces and image potential states, *Vacuum* **41**, 535 (1990).
- [27] L. Jurczyk and M. Stęćlicka, Barrier-resonance states in an external electric field, *Surf. Sci.* **266**, 141 (1992).
- [28] M. Nekovee and J. E. Inglesfield, Threshold Behaviour of Surface Density of States at the Vacuum Level, *Europhys. Lett.* **19**, 535 (1992).
- [29] P. M. Echenique, R. Berndt, E. V. Chulkov, Th. Fauster, A. Goldmann, and U. Höfer, Decay of electronic excitations at metal surfaces, *Surf. Sci. Rep.* **52**, 219 (2004).
- [30] M. Alducin, V. M. Silkin, J. I. Juaristi, and E. V. Chulkov, Energy loss of ions at metal surfaces: Band-structure effects, *Phys. Rev. A* **67**, 032903 (2003).
- [31] D. P. Dewangan and J. Eichler, Charge exchange in energetic ion-atom collisions, *Phys. Rep.* **247**, 59 (1994).
- [32] V. M. Silkin, J. M. Pitarke, E. V. Chulkov, and P. M. Echenique, Acoustic surface plasmons in the noble metals Cu, Ag, and Au, *Phys. Rev. B* **72**, 115435 (2005).
- [33] P. A. Macri, J. E. Miraglia, and M. S. Gravielle, Ionization of hydrogen targets by short laser pulses, *J. Opt. Soc. Am. B* **20**, 1801 (2003).
- [34] C. Lemell, X.-M. Tong, F. Krausz, and J. Burgdorfer, Electron Emission from Metal Surfaces by Ultrashort Pulses: Determina-

- tion of the Carrier-Envelope Phase, [Phys. Rev. Lett. \*\*90\*\*, 076403 \(2003\)](#).
- [35] M. N. Faraggi, M. S. Gravielle, and V. M. Silkin, Quantum-mechanical model for valence-electron emission from metal surfaces, [Phys. Rev. A \*\*69\*\*, 042901 \(2004\)](#).
- [36] D. R. Penn, Electron mean-free-path calculations using a model dielectric function, [Phys. Rev. B \*\*35\*\*, 482 \(1987\)](#).
- [37] V. D. Rodríguez, E. Cormier, and R. Gayet, Ionization by short uv laser pulses: Secondary above-threshold-ionization peaks of the electron spectrum investigated through a modified Coulomb-Volkov approach, [Phys. Rev. A \*\*69\*\*, 053402 \(2004\)](#).